



Delft University of Technology

UAV-aided weather radar calibration

Yin, Jiapeng; Hoogeboom, Peter; Unal, Christine; Russchenberg, Herman; Van Der Zwan, Fred; Oudejans, Erik

DOI

[10.1109/TGRS.2019.2933912](https://doi.org/10.1109/TGRS.2019.2933912)

Publication date

2019

Document Version

Final published version

Published in

IEEE Transactions on Geoscience and Remote Sensing

Citation (APA)

Yin, J., Hoogeboom, P., Unal, C., Russchenberg, H., Van Der Zwan, F., & Oudejans, E. (2019). UAV-aided weather radar calibration. *IEEE Transactions on Geoscience and Remote Sensing*, 57(12), 10362-10375. Article 8818617. <https://doi.org/10.1109/TGRS.2019.2933912>

Important note

To cite this publication, please use the final published version (if applicable). Please check the document version above.

Copyright

Other than for strictly personal use, it is not permitted to download, forward or distribute the text or part of it, without the consent of the author(s) and/or copyright holder(s), unless the work is under an open content license such as Creative Commons.

Takedown policy

Please contact us and provide details if you believe this document breaches copyrights. We will remove access to the work immediately and investigate your claim.

Green Open Access added to TU Delft Institutional Repository

'You share, we take care!' – Taverne project

<https://www.openaccess.nl/en/you-share-we-take-care>

Otherwise as indicated in the copyright section: the publisher is the copyright holder of this work and the author uses the Dutch legislation to make this work public.

UAV-Aided Weather Radar Calibration

Jiapeng Yin¹, *Student Member, IEEE*, Peter Hoozeboom, Christine Unal, Herman Russchenberg²,
Fred van der Zwan, and Erik Oudejans

Abstract—Weather radar is well recognized as an effective sensor for obtaining the microphysical and dynamical properties of precipitation at high spatial and temporal resolution. Radar calibration is one of the most important prerequisites for achieving accurate observations. In this article, a portable, cost-effective and repeatable radar calibration technique, namely, unmanned aerial vehicle (UAV)-aided radar calibration, is proposed. A UAV serves as the stable aerial platform carrying a metal sphere, flying over the radar illumination areas to complete the calibration process. The flying routine of the UAV can be pre-programmed, and thus, the antenna pattern regarding different elevation and azimuth angles can be retrieved. To obtain the position of the sphere, the real-time single-frequency precise point positioning-type global navigation satellite system solution is developed. In addition, the radar constant is calculated in the range-Doppler domain, and only the data where the metal sphere separates from clutter and other objects are selected. The S-band polarimetric Doppler transportable atmospheric radar (TARA) is used in the calibration campaign. The experiments demonstrate the following results: 1) antenna pointing calibration can be completed and 2) antenna pattern can be retrieved and weather radar constant can be accurately calculated.

Index Terms—Antenna pattern retrieval, antenna pointing calibration, unmanned aerial vehicle (UAV)-aided radar calibration, weather radar.

I. INTRODUCTION

WEATHER radar is well recognized as an indispensable tool for atmospheric observation because it obtains the information of atmospheric phenomena at a large scale within a short time [1]. According to different atmospheric applications, various types of radars in different configurations and platforms can be used. The key to using weather radar data is the sufficient measurement accuracy. However, radar system bias can be introduced from any radar component, which adds to the inestimable uncertainty in radar measurements. This system bias should be quantified through the process of “radar calibration,” which aims to identify the unknown system error caused by the transmitter, receiver, and antenna by using some

standard objects [2]. The system errors can be estimated by inserting the test signal into the radar system or by using objects with known scattering property. The radar calibration can be divided into two parts: the internal calibration and the external calibration.

For the internal calibration, built-in test equipment is installed to act as the internal radar calibration loop to monitor the variability of the electronic components inside the radar system. However, since the radar system has many discrete components, it is difficult to characterize every component. Internal calibration can help to measure the calibration drifts over time. These drifts are caused by the gradual degradation of the system performance (e.g., gain and loss in the transmitter and receiver), but not including the antenna (e.g., radome changes) [3]. Hence, it may be more practical to evaluate and characterize the radar system as a whole using the external calibration. As for the internal calibration, it can be used to monitor the stability of the transmitter and receiver.

The external calibration, always regarded as end-to-end calibration, involves the measurement of backscattering of a calibrator with known radar cross section (RCS), such as a trihedral reflector or metal sphere. To characterize the radar system error, an external calibration that covers the full path of the transmitter, receiver, and antenna is necessary. The current external calibration technique is mainly using a tethered balloon hanging metal sphere [4] or trihedral locating on the top of a tower or mast [5]. However, there are some shortcomings with these methods. First, these methods are limited due to location. When conducting the external calibration, the calibrator needs to be positioned in the far field, which seems impossible for some radars located at the top of high buildings or towers. Second, it is expensive to set up a tower or purchase a helium balloon. Third, it is not easy to repeat the calibration process due to the inconvenience of the calibration equipment transportation. Also, for vertically pointing cloud radar or other radar with mechanical constraints, these calibration methods cannot be applied. Hence, it is important to find a portable, cost-effective and repeatable solution that replaces or complements the current methods.

We present a novel calibration method to solve the aforementioned problems. The solution uses an unmanned aerial vehicle (UAV) as the platform to carry a metal sphere to achieve the external radar calibration. This idea was initially proposed during the Aerosol, Clouds, and Trace gases (ACTRIS) workshop held in Cologne, Germany, in 2015, in which the current and planned calibration methods as well as radar calibration phase classification were discussed [6]. Inspired by the workshop, a

Manuscript received January 31, 2019; revised May 22, 2019; accepted July 12, 2019. Date of publication August 28, 2019; date of current version November 25, 2019. (*Corresponding author: Jiapeng Yin.*)

J. Yin is with the College of Electronic Science, National University of Defense Technology, Changsha 410073, China, and also with the Department of Geoscience and Remote Sensing, Delft University of Technology, 2628 Delft, The Netherlands (e-mail: j.yin@tudelft.nl).

P. Hoozeboom, C. Unal, H. Russchenberg, F. van der Zwan, and E. Oudejans are with the Department of Geoscience and Remote Sensing, Delft University of Technology, 2628 CN Delft, The Netherlands (e-mail: p.hoozeboom@tudelft.nl; c.m.h.unal@tudelft.nl; h.w.j.russchenberg@tudelft.nl).

Color versions of one or more of the figures in this article are available online at <http://ieeexplore.ieee.org>.

Digital Object Identifier 10.1109/TGRS.2019.2933912

0196-2892 © 2019 IEEE. Personal use is permitted, but republication/redistribution requires IEEE permission.
See http://www.ieee.org/publications_standards/publications/rights/index.html for more information.

UAV-aided external calibration technique was proposed to calibrate a dual intermediate-frequency frequency-modulated continuous-wave (FMCW) radar [7]. This Ku-band radar was developed to detect targets with small RCS (e.g., drone). However, the antenna pointing calibration has not been done and the influence of the antenna pattern was not fully discussed. Duthoit *et al.* [8] introduced the operation and scanning modes for antenna characterization and radar calibration, focusing more on the concept description; however, the quantitative results were not provided.

In this article, the radar calibration technique is specifically designed for weather radar by considering the antenna pointing calibration, antenna pattern retrieval, and calibration error quantification. Compared with other types of radar, weather radar aims to measure volume distributed targets (i.e., precipitation) where quantitative backscattering measurements of hydrometers are required. Thus, antenna pointing calibration is important because the location of the measured resolution volume of which backscattering is estimated should be known. The antenna pattern retrieval is also necessary for accurate quantification due to the fact that the radar constant of weather radar is related to the antenna pattern integration. Finally, the robustness of the proposed technique can be proved through the calibration error quantification.

The article is organized as follows. Section II provides the basic principles, including weather radar equation, calibration configuration, and sphere positioning. The calibration measurements and their analyses are provided in Section III, in which the UAV flying mode and radar measurements, antenna pointing calibration, along with antenna pattern fit are discussed. Section IV presents the experimental results and discussion, containing the antenna constant and radar constant. Some conclusions are drawn in Section V.

II. BASIC PRINCIPLES

A. Weather Radar Equation

Weather radar is designed to sample distributed targets, such as precipitation, and its range equation is [1]

$$P_r(R) = \left[\frac{P_t G_0^2 \rho}{\lambda^2 (4\pi)^3} \right] \left(\int \int f^2(\theta, \phi) d\Omega \right) \frac{\pi^5 |K_w|^2 Z(R)}{R^2} \cdot \frac{1}{L} \cdot 10^{-18} \quad (1)$$

where $P_r(R)$ is the received power in range R , P_t is the transmitter power, G_0 is the peak boresight gain of the antenna, ρ is the range resolution, λ is the radar wavelength, $f(\theta, \phi)$ is the normalized antenna pattern function versus elevation and azimuth angles (θ, ϕ) , $|K_w|^2$ is the dielectric factor of water, and $Z(R)$ is the equivalent reflectivity factor in range R . L is the total loss of the radar system.

Equation (1) can also be reformulated as

$$Z(R) = C \cdot P_r \cdot R^2 \quad (2)$$

where C is the radar constant, which is expressed as

$$C = \frac{\lambda^2}{\pi^5 |K_w|^2} \left[\frac{(4\pi)^3}{P_t G_0^2 \rho} \right] \left(\frac{1}{\int \int f^2(\theta, \phi) d\Omega} \right) \cdot L \cdot 10^{18} \quad (3)$$

For radar calibration, the estimation of the radar constant C can be obtained by measuring P_r and R corresponding to a calibrator whose Z is known. The calibrator can be a metal sphere for the reason that its RCS is independent of incidence angle. A sphere or other calibrators, however, is a point target rather than a distributed target, and the equivalent RCS of a sphere treated as a distributed target will be derived next.

The total loss L in (3) includes all the hardware and processing loss. The hardware loss can be quantified by inspecting each radar component; nevertheless, the coupling between the radar components (part of hardware loss) and the processing loss is difficult to estimate. This article proposes a technique to calculate the radar constant without estimating the total loss.

However, the impact of the range resolution on the total loss L will be investigated. The reason is that in our case, the transportable atmospheric radar (TARA) is calibrated using a higher range resolution (e.g., 3 m) than the operational one (e.g., 30 m) since the higher range resolution is required for practical reasons (see Section II-B). The radar constant estimated in a higher range resolution can be used for radar configured in other range resolutions with proper adjustment. The loss L may vary due to different range resolutions.

In the case of a distributed target, as shown in Fig. 1(a), the average received power $\bar{P}_{r,\text{dis}}$ can be expressed as

$$\bar{P}_{r,\text{dis}} = \frac{P_t G_0^2 \lambda^2}{(4\pi)^3 R_{\text{dis}}^2} \cdot \frac{\sigma_{\text{dis}} \rho_{\text{dis}}}{L_{\text{dis}}} \left(\int \int f^2(\theta, \phi) d\Omega \right) \quad (4)$$

where R_{dis} is the range of the distributed target, σ_{dis} is the backscatter cross section per unit volume ($\text{m}^2 \text{m}^{-3}$) of the distributed target, ρ_{dis} is the range resolution determined by the distance between the -3 dB points on the main lobe of the range transfer function [9], and L_{dis} is the total loss of radar system in this case.

Equation (4) can be verified if the distributed target is replaced by several point targets which, for instance, are separated by $\rho_{\text{dis}}/2$, as shown in Fig. 1(b). In this case, three point targets with RCS σ_{sp} contribute to the received power after the convolution with the radar transfer function. Their powers are summed, and the received power is approximately two times as large as a single point target. Specifically, in such situation, the equivalent σ_{dis} of a distributed target is related to $2\sigma_{\text{sp}}/\rho_{\text{dis}}$, which means that when using point targets for weather radar calibration, the range resolution should be known.

Furthermore, if only one point target (i.e., one sphere) is considered, as shown in Fig. 1(c), the conventional radar equation of point target, referred to as the peak response, is defined as

$$P_{r,\text{sp}}^{\text{max}} = \frac{P_t G_0^2 \lambda^2 \sigma_{\text{sp}}}{(4\pi)^3 R_{\text{sp}}^4} \cdot \frac{1}{L_{\text{sp}}} \quad (5)$$

where $P_{r,\text{sp}}^{\text{max}}$ is the peak power, σ_{sp} is the RCS of the sphere, R_{sp} is the range of the sphere, and L_{sp} is the total loss of radar system in this case. The estimation of the range resolution ρ_{sp} is problematic because of the non-ideal condition of radar receiver bandwidth. As shown in Fig. 1(c), the real radar transfer function deviates from the ideal one, making the

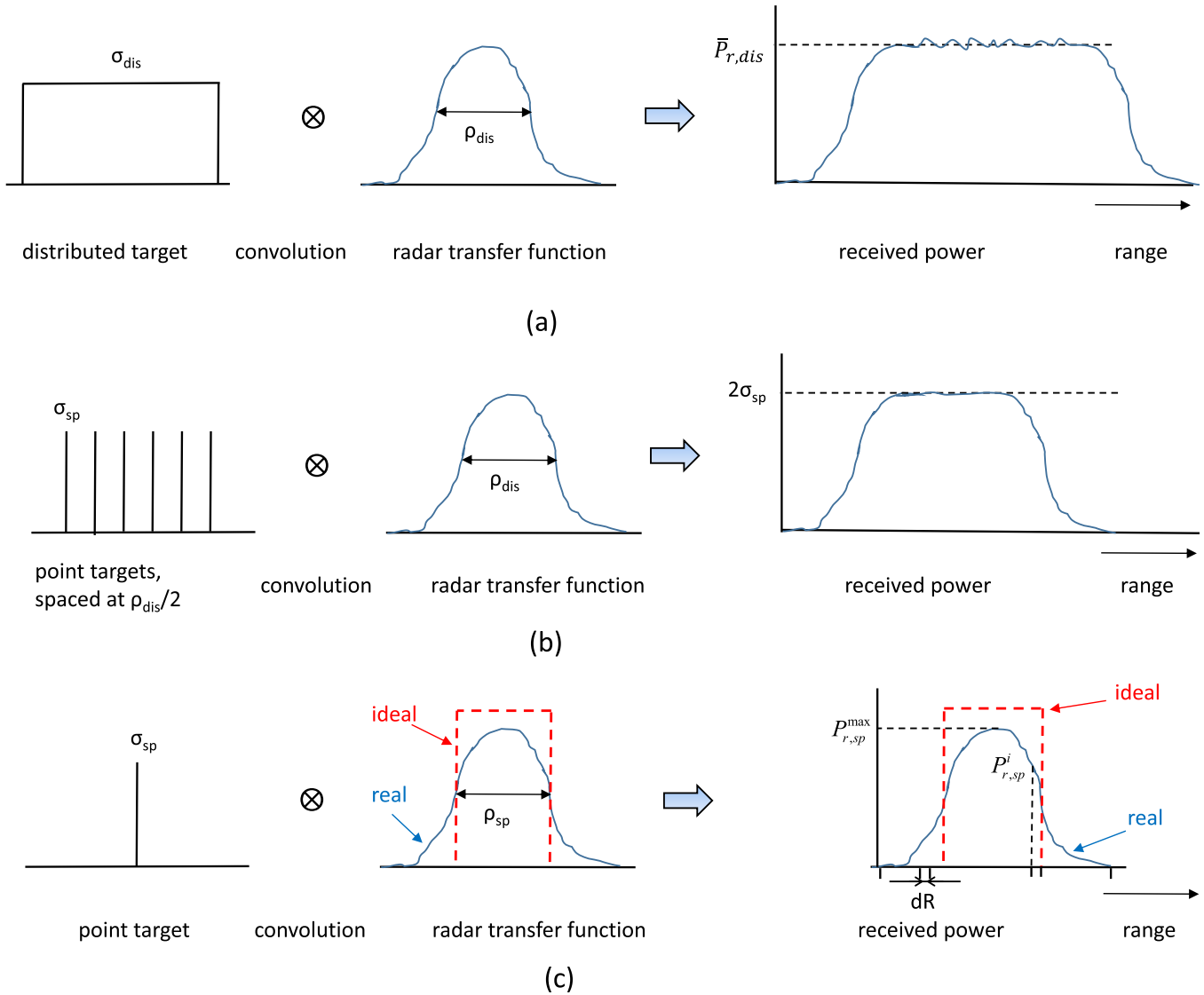


Fig. 1. Radar response of distributed target and point target. (a) Distributed target. (b) Several point targets mimic a distributed target. (c) Point target.

measured peak power $P_{r,sp}^{\max}$ deviate from the ideal peak power and such deviation cannot be quantified.

In addition, for an FMCW radar, the range information is obtained by the Fourier transform of the beat signal. When the target is moving during the measurements, the Fourier transform leakage leads to energy distribution in neighboring range gates. Therefore, the measured peak power method will underestimate the backscattering of the sphere.

To alleviate the problem of non-ideal radar transfer function and the Fourier transform leakage in the FMCW radar, we consider the integrated response. Specifically, following the energy conservation theorem, for any actual range resolution ρ_{sp} , the integrated power $P_{r,sp}^I$ can be expressed as

$$P_{r,sp}^I = \int_0^{\infty} P_{r,sp}(R) dR = \frac{P_t G_0^2 \lambda^2 \sigma_{sp}}{(4\pi)^3 R_{sp}^4} \cdot \frac{\rho_{sp}}{L_{sp}} \quad (6)$$

where $P_{r,sp}(R)$ is the received power in the function of different ranges. The integral form in (6) can be approximated

by the numerical form as

$$P_{r,sp}^I = \sum_i P_{r,sp}^i dR \quad (7)$$

where $P_{r,sp}^i$ is the i th received power sampled by the sampling distance dR (i.e., the specified range resolution). Thus, the integrated power instead of the peak power is recommended in the weather radar constant calculation.

It is also worth noting that the angular dependence of the term $P_{r,sp}^I R_{sp}^4$ is related to the two-way antenna gain. Therefore, this term will be used afterward to represent the two-way antenna gain. By combining (3) with (6), we obtain the radar constant C^I (the superscript I relates to the integrated antenna pattern)

$$C^I = \frac{\lambda^4}{\pi^5 |K_w|^2} \left[\frac{\sigma_{sp}}{P_{r,sp}^I R_{sp}^4} \right] \frac{L \rho_{sp}}{L_{sp} \rho} \left(\frac{1}{\int \int f^2(\theta, \phi) d\Omega} \right) 10^{18}. \quad (8)$$

Hereby, we define the loss-over-range-resolution ratio as

$$r_{L\rho} = \frac{L\rho_{\text{sp}}}{L_{\text{sp}}\rho}. \quad (9)$$

Then, (8) can be expressed as

$$C^I = \frac{\lambda^4}{\pi^5 |K_w|^2} \left[\frac{\sigma_{\text{sp}}}{P_{r,\text{sp}}^I R_{\text{sp}}^4} \right] r_{L\rho} \left(\frac{1}{\int \int f^2(\theta, \phi) d\Omega} \right) 10^{18}. \quad (10)$$

The value of $r_{L\rho}$ equals to 1 when the same range resolution is used for calibration and atmospheric measurements, which is of course the preferable option. Otherwise, the value of $r_{L\rho}$ can be quantified by the measurements of a distributed target (i.e., precipitation) at the same range R but with the range resolution setting ρ and ρ_{sp} , and the corresponding received powers are

$$\bar{P}_{r,\rho} = \frac{P_t G_0^2 \lambda^2}{(4\pi)^3 R^2} \cdot \frac{\sigma_{\text{dis}} \rho}{L} \left(\int \int f^2(\theta, \phi) d\Omega \right) \quad (11)$$

$$\bar{P}_{r,\rho_{\text{sp}}} = \frac{P_t G_0^2 \lambda^2}{(4\pi)^3 R^2} \cdot \frac{\sigma_{\text{dis}} \rho_{\text{sp}}}{L_{\text{sp}}} \left(\int \int f^2(\theta, \phi) d\Omega \right) \quad (12)$$

where σ_{dis} is the backscatter cross section per unit volume ($\text{m}^2 \text{m}^{-3}$) of precipitation (the precipitation is assumed to be homogeneous in the measurement period). Combining (11) and (12), the loss-over-range-resolution ratio can be estimated by

$$r_{L\rho} = \frac{\bar{P}_{r,\rho_{\text{sp}}}}{\bar{P}_{r,\rho}}. \quad (13)$$

When the assumption is made that the antenna pattern can be approximated by a Gaussian function [1], the radar constant is expressed as C^A (the superscript A relates to the approximated antenna pattern)

$$C^A = \frac{\lambda^4}{\pi^5 |K_w|^2} \left[\frac{\sigma_{\text{sp}}}{P_{r,\text{sp}}^I R_{\text{sp}}^4} \right] r_{L\rho} \left(\frac{8 \ln 2}{\pi \theta_1 \phi_1} \right) 10^{18} \quad (14)$$

where θ_1 and ϕ_1 are the 3-dB beamwidths. Hereby, the antenna constant A is defined, which represents the contribution of the antenna in the radar constant calculation, and corresponding to (10) and (14), we have

$$A^I = 1 / \int \int f^2(\theta, \phi) d\Omega \quad (15)$$

$$A^A = 8 \ln 2 / \pi \theta_1 \phi_1. \quad (16)$$

The antenna and radar constants are calculated based on field measurements. In this article, two different measurements, namely, from UAV and transponder, are used to calculate the corresponding values. For the terminology with respect to antenna constant and radar constant, we will have A_y^x and C_y^x , where x is I or A (the integrated or approximated antenna pattern) and y is UAV or ref (the measurements are from the UAV- or transponder-aided calibration experiments). The antenna beam pattern measurements using a transponder [10] can be considered as a reference to evaluate the performance of the proposed UAV-aided radar calibration technique.

In addition, radar calibration is used to identify the uncertainty in the radar constant, and in this article, C^I is the target radar constant, whose uncertainty is expressed as

$$\frac{\delta C^I}{C^I} = \sqrt{\left(\frac{\delta \sigma_{\text{sp}}}{\sigma_{\text{sp}}} \right)^2 + \left(\frac{\delta P_{r,\text{sp}}^I}{P_{r,\text{sp}}^I} \right)^2 + 16 \cdot \left(\frac{\delta R_{\text{sp}}}{R_{\text{sp}}} \right)^2 + \left(\frac{\delta A^I}{A^I} \right)^2 + \left(\frac{\delta r_{L\rho}}{r_{L\rho}} \right)^2} \quad (17)$$

where $\delta X/X$ means the relative error of variable X . Note that the terms in (17) are all in linear scale. Combined with radar measurements, more details will be provided in Section IV-B.

Since the radar constant shown in (10) is related to a specific volume, it is necessary to know where the volume locates, which is the antenna pointing accuracy. This can be done by either fixing the antenna pointing to one direction and making the calibrator (e.g., metal sphere) move along the elevation or azimuth angle axis or fixing the calibrator and scanning the radar antenna along the elevation or azimuth angle direction. Due to the mechanical limitation of the radar used, the former is selected in this article. Considering the azimuth angle of the radar antenna pointing as an example, when the calibrator moves continuously from sidelobe to main lobe and then to sidelobe of the antenna pattern in different elevation angles, the measured $P_{r,\text{sp}}^I R_{\text{sp}}^4$ term will approximate the antenna pattern. It is expected that when all the peaks of $P_{r,\text{sp}}^I R_{\text{sp}}^4$ are chosen and outputting their azimuth and elevation angles in the azimuth–elevation plane, they tend to have the same azimuth angle but different elevation angles. The averaged azimuth angle deviating from 0° is regarded as the azimuth offset. A similar work can be done to estimate the elevation angle of the antenna pointing.

When the antenna pointing calibration is done, the $P_{r,\text{sp}}^I R_{\text{sp}}^4$ values measured in different elevation and azimuth angles are used to interpolate the antenna pattern. With the retrieved antenna pattern, the antenna constant in (15) can be obtained. It is expected that the radar constant C^I based on the antenna integration is more accurate than the conventional one (i.e., the approximated C^A) and the reasons are twofold. One is that C^I is based on real measurements and C^A relies on a model-based approximation. The other reason is that enough measurements are used in C^I to eliminate some random variations. More results are given in Section IV-B to support such statement.

B. Calibration Configuration

In the Cabauw Experimental Site for Atmospheric Research (CESAR) observatory, The Netherlands, there are two FMCW radars, one S-band TARA and one X-band IRCTR Drizzle Radar (IDRA) [11], [12]. The two radars were designed by the Delft University of Technology for atmospheric research, and their measurements are displayed online in real-time. The data provide a long-term observation to monitor the trends of precipitation changes. Particularly, TARA is considered in the calibration campaign, and its specifications are shown in Table I. In addition, the boresight cut of

TABLE I
S-BAND RADAR TARA SPECIFICATIONS

Radar	TARA
Type	FMCW radar (solid state)
Frequency	3.298 GHz
Transmit power	100 W
Antenna diameter	3 m (parabolic)
Beam width	2.1°
1 st side lobe	-20 dB
Polarization	HH/HV/VV
pulse repetition frequency	2 KHz
Bandwidth	2 - 50 MHz
Antenna rotation	Elevation 0°- 90°, Azimuth fixed

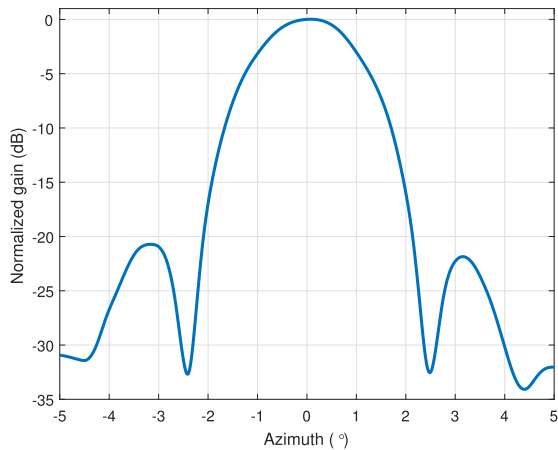


Fig. 2. TARA one-way antenna beam pattern obtained by a radar transponder.

TABLE II
UAV SPECIFICATIONS

MATRICE 600	Manufacturer: DJI, China
Type	Micro-drone hexacopter
Dimension	Diameter 167 cm, height 62 cm
Weight	9.1 kg with batteries
Payload	Max 6 kg
Flight mode	Automatic with waypoint or based on radio control
Hovering Accuracy	P-Mode: Vertical ± 0.5 m, Horizontal ± 1.5 m
Max Speed	18 m/s (No wind)
Endurance	No payload: 35 min, 6 kg payload: 16 min

the antenna beam pattern of TARA along the azimuth direction measured by a radar transponder [10] is shown in Fig. 2. This is the one-way antenna pattern. A similar pattern is obtained along the elevation axis. Therefore, $\theta_1 \approx \phi_1$ for TARA and estimated to be 2.1°, which will be used in (16) to calculate the antenna constant. The transponder-aided radar calibration experiment took place after TARA was built in 1999.

During the radar calibration campaign, a UAV named DJI Matrice 600 served as the stable aerial platform carrying a metal sphere, flying over the radar illumination areas to complete the calibration process. The UAV is shown in Fig. 3(a) where the UAV was placed on the ground next to a metal sphere, and the specifications of the UAV are shown in Table II. This is a powerful UAV with a maximum payload

of 6 kg. The UAV should fly at small speed to guarantee the data quality for TARA Doppler processing, and we choose the minimum flying velocity (1 m/s^{-1}). In addition, there is GPS onboard and the positioning accuracy is in meter, which fulfills the requirement for radar ranging. GPS information in the UAV can be used to calculate the distance between the sphere and the radar R_{sp} when the connecting line between the UAV and sphere is short enough. However, to avoid the backscattering of UAV contaminating that of the sphere in the radar measurements, the connecting line should be long enough to separate the UAV from the sphere in different range bins. In this case, an external GPS box, which is located underneath the sphere, is required. The connecting line between the UAV and the sphere and that between the sphere and the external GPS device is set to the same. Thus, the coordinates of the sphere can be retrieved with the coordinate outputs of GPS on UAV and external GPS box. The details of the external GPS device will be given later. Sometimes, due to the influence of wind, UAV, sphere, and external GPS may not be one line, which results in sphere positioning errors. Therefore, the calibration campaign requires quiet meteorological conditions: weak wind and no precipitation.

The UAV-aided radar calibration diagram is shown in Fig. 4. The legal UAV flying height in The Netherlands is 120 m, and the sphere should be placed in the far field (i.e., 350 m). Thus, during the experiment, TARA was configured with the elevation angle 12° and the connecting line length was 50 m. The connecting line between the UAV and the sphere was a fishing line that is light and firm. With a proper flying routine design, the sphere can only be placed in the antenna main beam, while UAV and external GPS device are outside of the main beam. However, this may not be enough, because when the sphere RCS is much less than the UAV RCS, the contamination of UAV coming from antenna sidelobe will still affect the backscattering of the sphere. The high-resolution mode (i.e., 3 m) guarantees a clear range separation between the backscattering of the UAV, sphere, and GPS box, which can be observed in Section III-A. Based on this reason, the calibration campaign is now conducted in the high-resolution mode instead of operational mode (i.e., 30 m). The scene of the calibration is shown in Fig. 3(c), where UAV, metal sphere, and GPS box are visible from top to bottom in the sky.

C. Sphere Positioning

The range R_{sp} can be obtained through various global navigation satellite system (GNSS) processing techniques. Some of the most precise positioning techniques consist of differential GNSS solutions. For differential solutions, the spatial stability of major GNSS signal delay sources, such as the troposphere and ionosphere, is necessary. For this assumption to hold, we are dependent on a moderate to short baseline. Introducing such a baseline dependence means that the user would either need to operate their own base station or use a nearby permanent GNSS station, for instance, those linked to the IGS GNSS network [13]. This is not always the most practical solution, especially for the calibration of mobile radar

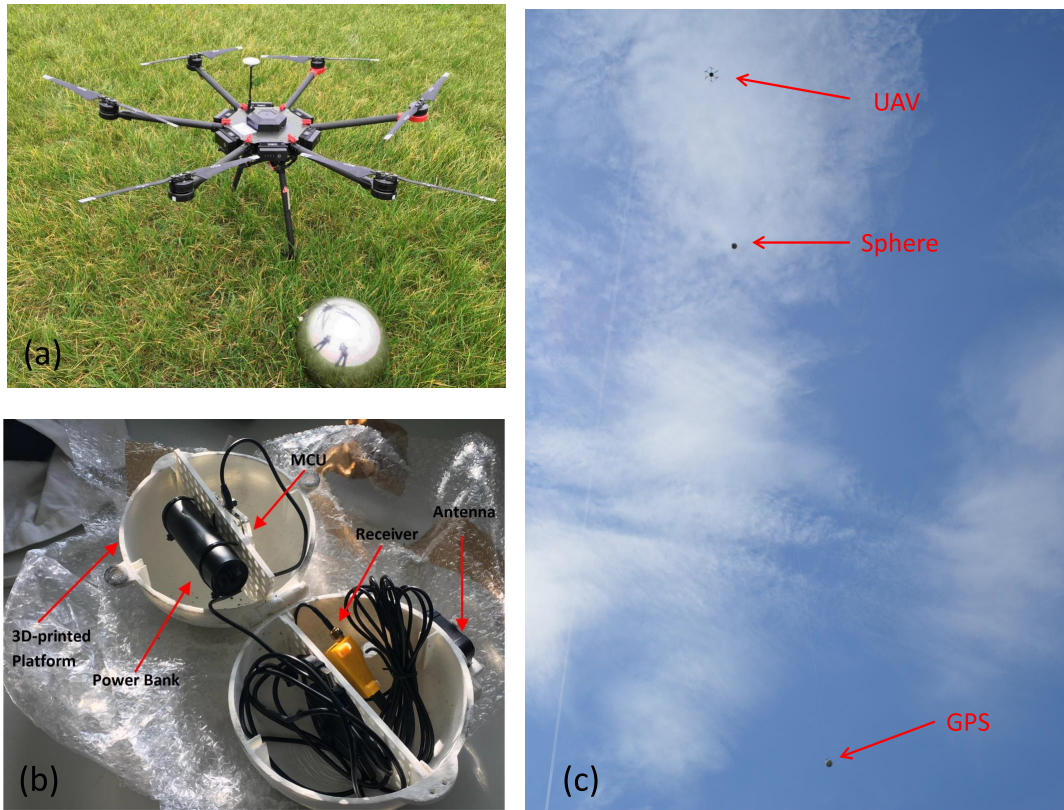


Fig. 3. Calibration hardware and setup. (a) UAV DJI Matrice 600 and the metal sphere. (b) External GPS box. (c) Scene of UAV, sphere, and external GPS box.

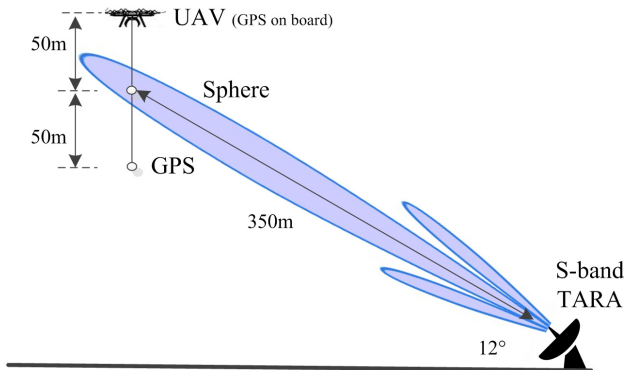


Fig. 4. Schematic of UAV-aided radar calibration technique.

systems. Therefore, we adapted the real-time single-frequency precise point positioning (RTSFPPP) algorithm developed at the Mathematical Geodesy and Positioning Group, Delft University of Technology [14]. Instead of making use of a base station, we rely on a broad network of permanent stations through which we obtain the predicted satellite orbits, predicted global ionospheric maps, and real-time satellite clock corrections. We expect a position standard deviation of 0.15 m in the horizontal direction and 0.30 m in the vertical direction. Although RTSFPPP can be used in real-time, in the light of this article, post-processing is used.

The hardware of the external GPS box is shown in Fig. 3(b), and the details of each component are shown in Table III.

TABLE III
GNSS POSITIONING HARDWARE

Part	Specification
MCU	Raspberry Pi 2
Power	Anker powercore 1500 mAh
Receiver	Ublox M8T
Receiver case	Custom 3D-printed
Antenna	Taoglass Magma X 171
Platform	Custom 3D-printed

All the components can be placed in the GNSS platform that is a custom 3-D-printed sphere. Our objective is to obtain a location-invariant calibration method. Therefore, we make sure that everyone can obtain our GNSS platform, the positioning is baseline independent, and the UAV software works off-line. In the future, all 3-D designs will be available online, and anyone who has the hardware at hand can be self-sufficient by using a 3-D printer.

III. CALIBRATION MEASUREMENTS AND ANALYSIS

A. UAV Flying Mode and Radar Measurements

A proper flight mode is designed to measure the antenna beam pattern. Since the flying routine of the UAV can be programmed in advance according to the input of the GPS coordinates, which is referred to the waypoint operational mode, the horizontal and vertical zigzag flying modes can be designed in the calibration campaign. The example of a

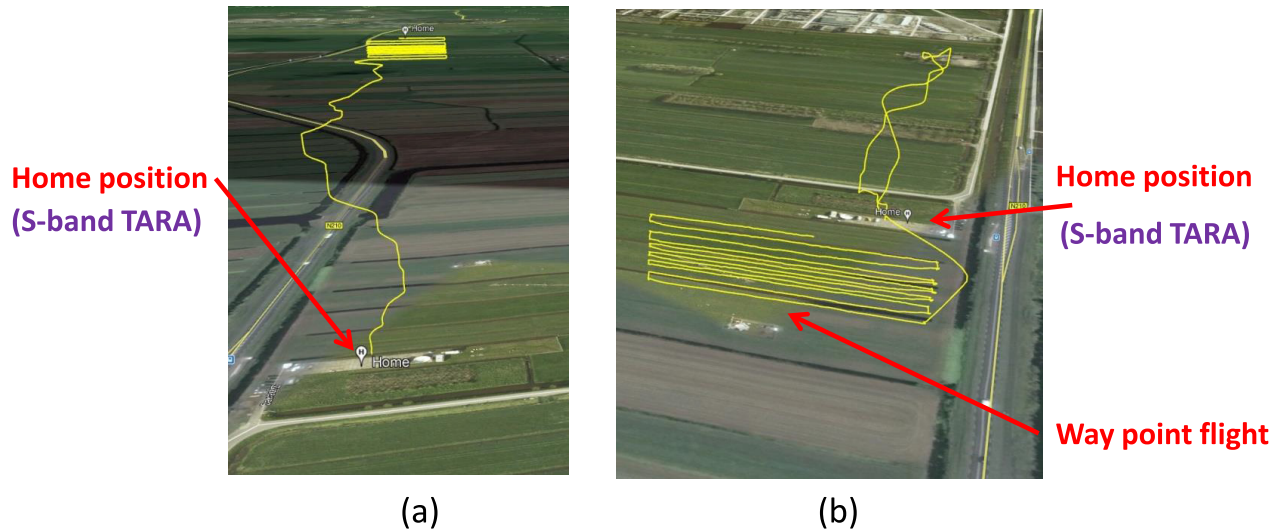


Fig. 5. Horizontal zigzag movement of the UAV. (a) Original. (b) Enlarged.

horizontal zigzag movement is shown in Fig. 5. The UAV starts at the home position where TARA locates and flies to the far field conducting the horizontal movement in the plane perpendicular to the antenna pointing direction. Each time the UAV reaches the programmed end left or right position, it will go down or go up several meters. The enlarged flight mode with the horizontal zigzag movement is shown in Fig. 5(b). For each horizontal flight routine in Fig. 5, the sphere moves with a fixed elevation angle and continuously changeable azimuth angles. With the completion of such movement, it is expected that if the antenna pattern can be approximated by the Gaussian function, the $P_{r,sp}^I R_{sp}^4$ term will also have a Gaussian shape because it relates to the antenna gain in different angles. Similarly, the vertical zigzag movements will generate several cuts along the elevation angles with a fixed azimuth angle. With the measured elevation, azimuth angles, as well as the $P_{r,sp}^I R_{sp}^4$ values, proper antenna pattern fitting methods can be used to obtain the 3-D antenna normalized gain, which will be discussed in Section III-C.

To better characterize the radar measurements, the measured signal is inspected in both time domain and frequency domain, as shown in Fig. 6. In addition, the GPS output of UAV (blue line), sphere (black line), and GPS box (red line) are shown in Fig. 6. The data discussed here are from the case with a vertical zigzag movement on March 6, 2018. First, when the measurements are observed in the time domain as shown in Fig. 6(a), the movements of UAV, sphere, and GPS box are visible. Fig. 6(a) shows a good match of the range information between the radar- and GPS-measured ones, sharing the same movement pattern but some range deviation. In this case, the mean and standard deviation of the sphere absolute range difference between the GPS-retrieved and the radar-measured ranges are 2.2 and 3.9 m, respectively.

Furthermore, some of the data are visualized in the frequency domain, which is obtained by taking 512 time samples in Fig. 6(a) and applying the Fourier transform at a fixed range. Specifically, the range-Doppler spectrogram of ray 156 is considered. As shown in Fig. 6(b), the top signature represents

the echoes from the UAV, which is consistent with the rotating blades of the UAV. In this case, the position of the sphere is indicated by a black line and the backscattering of the sphere is centered around 0 m/s. Moreover, we can see the echoes from the GPS box in the bottom of Fig. 6(b), indicated by the red line. The separation in the range of the UAV, sphere, and GPS box is sufficient; otherwise, the estimation of the backscattering from the sphere would be biased. The estimation of the backscattered power of the sphere is by taking one rectangular window in the spectral domain to integrate the entire sphere signature. Recall the statement in Section II-A, the integrated power is used to compensate the influence of the non-ideal radar transfer function and the Fourier transform leakage. Estimating the backscattered power of the sphere in the range-Doppler domain helps to eliminate the contamination from clutter, such as vehicle echoes as shown in Fig. 6(b). In addition, only the data related to the sphere, which are not contaminated by the ground clutter, are selected for the radar constant calculation. In practice, before the launch of the UAV, radar measurements of the environment are collected to quantify the clutter. These clutter measurements lead to the selection of the range of about 350 m. In the case of the TARA calibration, the signal-to-clutter ratio varies from 20 to 50 dB. The ground clutter contamination is not so severe compared with the backscattering of the sphere. Thus, we consider all the measurements, including the ones with the sphere located at 0 m/s⁻¹.

B. Antenna Pointing Calibration

The verification of antenna pointing is part of weather radar calibration. We consider another data set measured on May 15, 2018, with a sphere diameter of 20 cm, where the UAV flew at the velocity of 1 m/s with a horizontal zigzag flight followed by a vertical one. We transform the GPS coordinates to the azimuth and elevation angles in the radar line of sight and output them chronologically (from red points to green points), as shown in Fig. 7(a). For better visualization, one point for

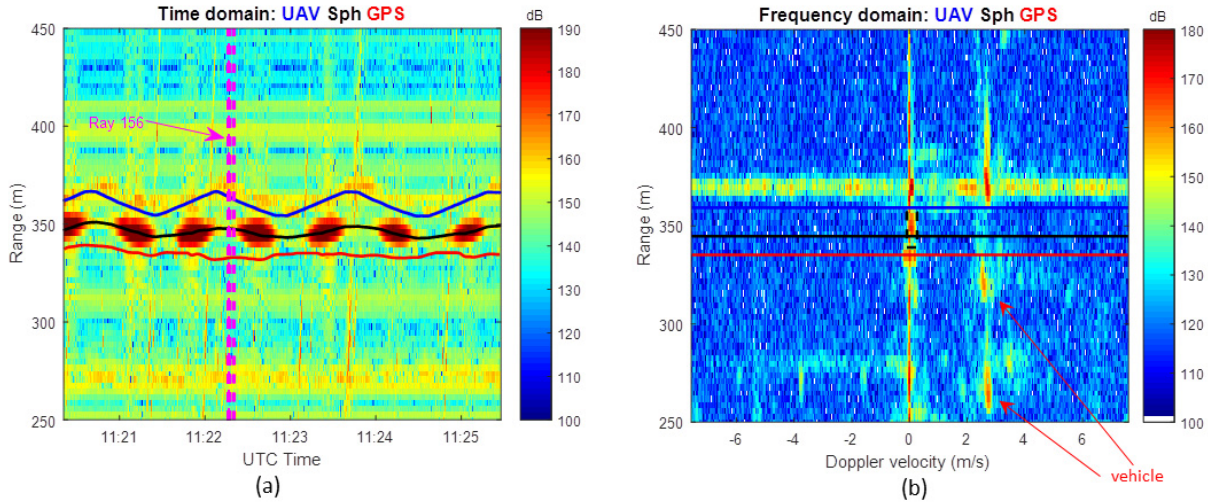


Fig. 6. Radar and GPS measurements of UAV, sphere, and GPS box. (a) Range-time image. (b) Range-Doppler spectrogram of ray 156.

every three GPS coordinates is shown. Since the data were obtained by both a horizontal and a vertical zigzag movement, it can be observed that there are several lines across the 3-dB antenna main beam (indicated as black dashed line) along both the azimuth and elevation axes, which is consistent with the designed flight. Those measurements close to the antenna main beam can be used to retrieve the antenna pattern. Accordingly, we calculate the variable $P_{r,sp}^I R_{sp}^4$, as shown in Fig. 7(b). From the frequency-domain derived results, several Gaussian-shaped patterns are visible. The left values of Fig. 7(b) are from the horizontal movement and the right ones are from the vertical flight. The difference between the maximum power value and the minimum power floor is around 50 dB. This means that the first antenna sidelobes are expected to be visible, but this is not so obvious. This is due to the short staying interval (not enough measurements) when the sphere is located in the antenna sidelobes.

Moreover, all the peaks related to the horizontal movement (left parts) are taken in Fig. 7(b) to output them in the azimuth–elevation plane, as shown in Fig. 7(c). It is observed that these peaks have very close azimuth angle but their elevation angles vary. Taking all the azimuth angles, the average angle is calculated as 0.1° , which means that the offset in azimuth is 0.1° . Similarly, all the peaks from the vertical movement (right parts) are taken in Fig. 7(b) and shown in Fig. 7(d). The calculated elevation offset is -0.2° . In addition, the same UAV flight mode is conducted by using a sphere of diameter 18 cm, and the calculated azimuth and the elevation angle offset are 0.1° and -0.3° , respectively. With the zigzag horizontally and vertically, it is concluded that the antenna pointing calibration for weather radar can be achieved.

C. Antenna Pattern Fit

With the radar-based $P_{r,sp}^I R_{sp}^4$ values and their corresponding GPS-based azimuth and elevation angles, it is possible to retrieve the antenna pattern. In the following analysis, all the values of $P_{r,sp}^I R_{sp}^4$ larger than 300 dB are taken for the antenna

pattern fitting. Note that the $P_{r,sp}^I R_{sp}^4$ measurements include the two-way (both transmit and receive) antenna pattern.

Considering the data measured from the horizontal movement on May 15, 2018, the retrieved antenna pattern is shown in Fig. 8. As shown in Fig. 8(a), the measured values are indicated by the blue circles, and the 2-D triangulation-based linear interpolation is conducted in MATLAB using the function named “griddata,” as shown in Fig. 8(b). The maximum point locates at $(0.1^\circ, -0.1^\circ)$ in the azimuth–elevation plane, as labeled with a blue filled circle. We recommend to take this angle point as the antenna pointing offset because antenna pointing has an impact on antenna pattern retrieval. Currently, we find that fitting results based on data from either horizontal movement or vertical movement are better than using combined data (both horizontal and vertical ones). In addition, Fig. 8(c) and (d) shows the sectional views of Fig. 8(b) with fixed elevation and azimuth angles, from which near-Gaussian shapes are observed. Compared with Fig. 8(d), Fig. 8(c) has a larger dynamic range and more complete antenna pattern, which is consistent with more measurements with a fixed elevation angle.

Furthermore, to qualitatively compare the antenna patterns (the UAV-aided and transponder-aided), we normalize the two-way interpolated antenna pattern of Fig. 8(c) (more reliable for the horizontal movement), compensate the azimuth offset, and shift it to the reference antenna pattern in Fig. 2. The result is shown in Fig. 8(e). A similar work has been done with the vertical movement and the outcome is shown in Fig. 8(f). We can observe that the derived antenna pattern fits quite well with the reference one. Since TARA is an FMCW radar with separate antennas, the fitting results show that the transmit and receive antennas have a good overlap at the place where the sphere is located. However, there are some antenna fitting deviations in the vertical movement, which may be caused by the sphere displacement due to different horizontal wind speed at different heights during the experiment. As shown in Fig. 7(a), the flying routine of the sphere in the vertical direction is not as straight as that in the horizontal direction.

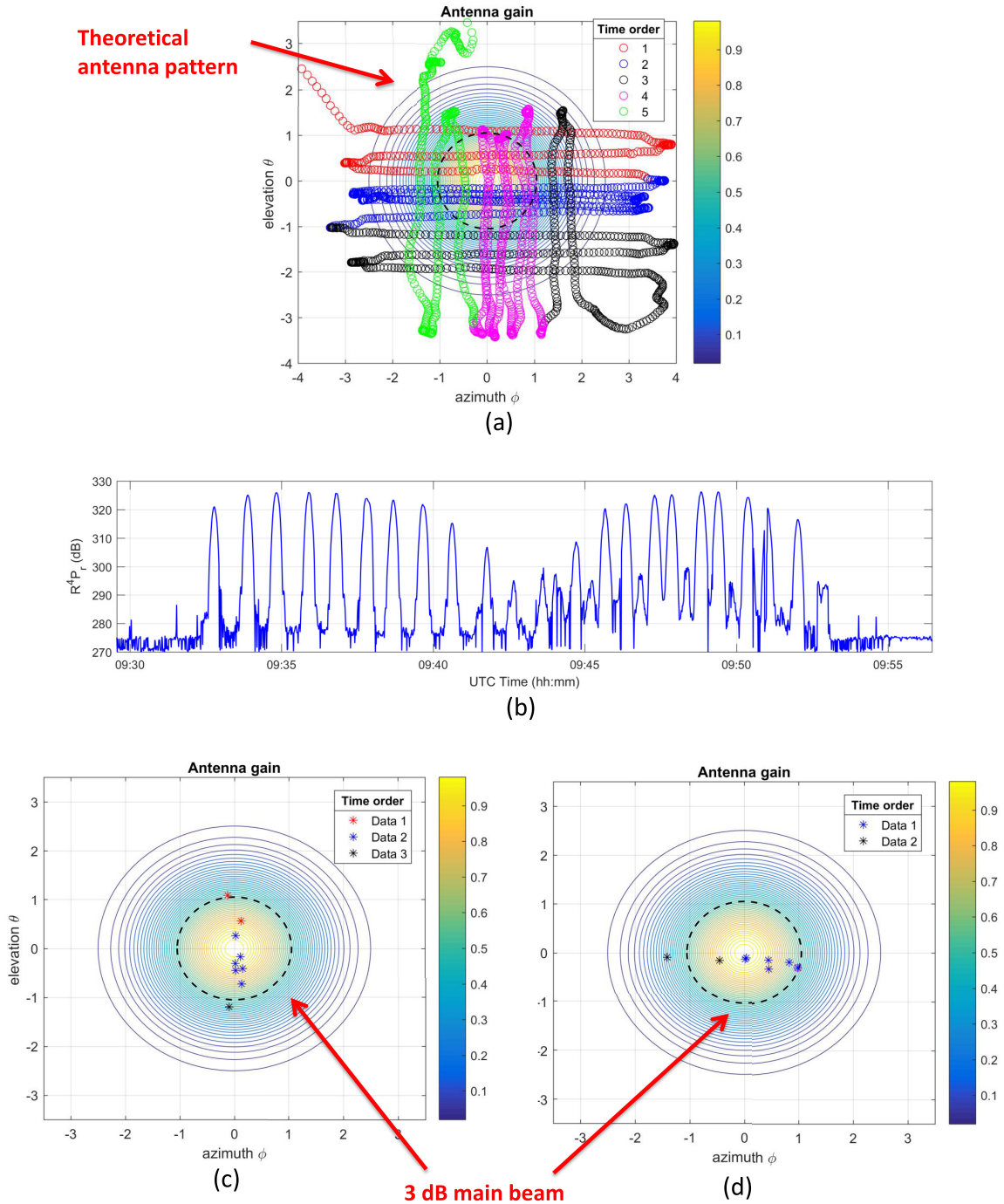


Fig. 7. GPS output and radar measurements of the sphere. (a) Azimuth and elevation angles. (b) $P_{r,sp}^I R_{sp}^4$ values. (c) Angles of $P_{r,sp}^I R_{sp}^4$ peak values of the horizontal movement. (d) Angles of $P_{r,sp}^I R_{sp}^4$ peak values of the vertical movement.

IV. EXPERIMENTAL RESULTS AND DISCUSSION

As mentioned in Section II-A, radar constants obtained from different range resolutions differ. In practice, radar calibration experiments require a high range resolution mode. This allows to easily separate the backscattering of the sphere from the backscattering of other targets, such as the UAV and the GPS box. With proper adjustment (i.e., estimating the loss-over-range-resolution ratio), the radar constant of the operational mode can be derived from the one of the high range resolution

modes. The following discussion is based on the radar measurements obtained in high range resolution (i.e., 3 m).

The relationship between the sphere diameters and the RCS for the TARA wavelength is shown in Fig. 9. During the whole experiments, we had spheres of diameter 9, 13, 18, 20, and 27 cm, which relate to the Mie scattering region. Different spheres were used in different experiments, and the campaign details and results are shown in Table IV. The calibration experiments were conducted for four days of the occasional

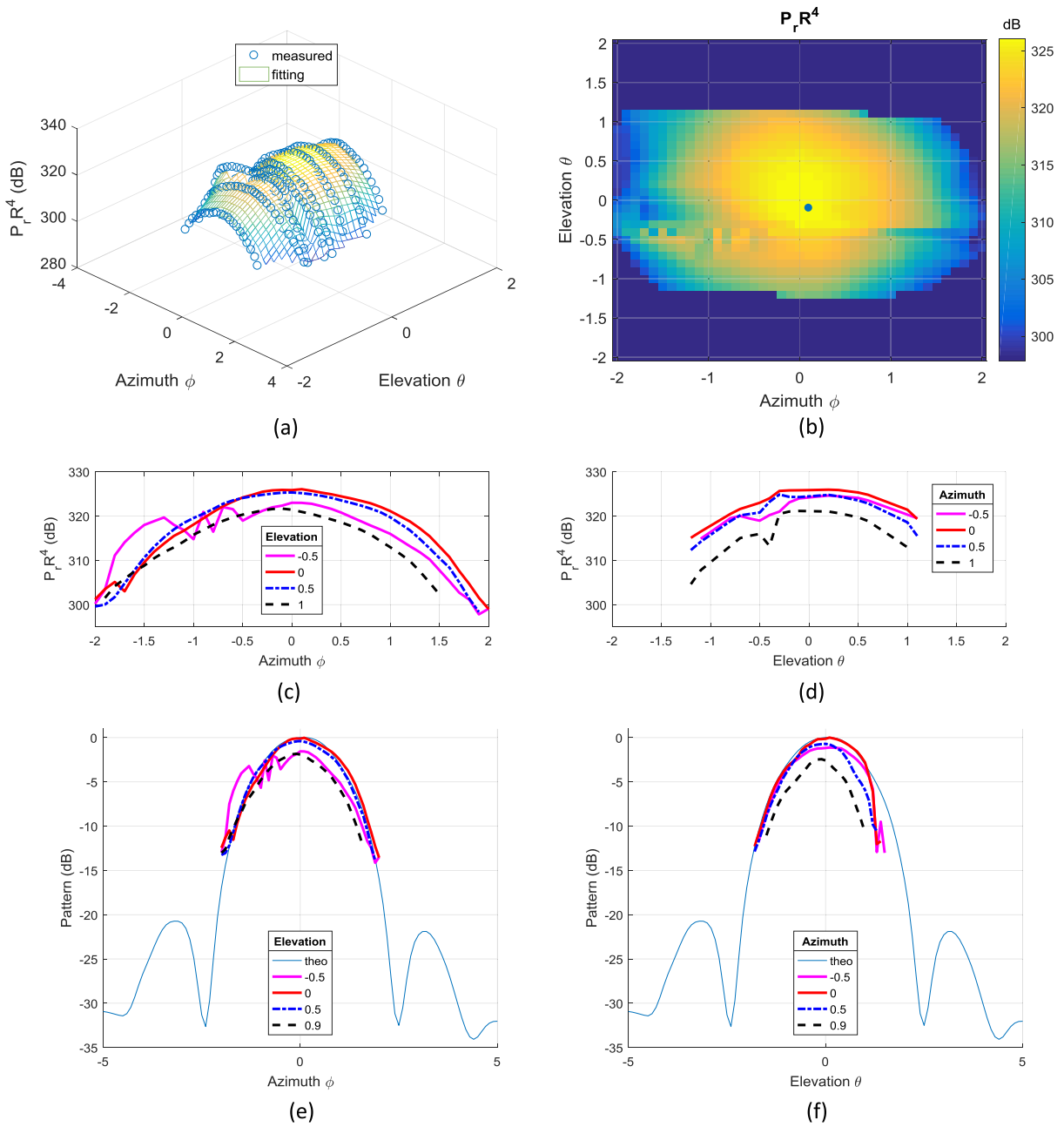


Fig. 8. 2-D antenna pattern fit. (a) 3-D view of measured and interpolated values. (b) 2-D view of interpolated values. (c) Sectional view of interpolated two-way antenna pattern with fixed elevation angles. (d) Sectional view of interpolated two-way antenna pattern with fixed azimuth angles. (e) Interpolated one-way antenna pattern fits the reference one with fixed elevation angles. (f) Interpolated one-way antenna pattern fits the reference one with fixed azimuth angles.

measurements of seven months; nevertheless, several measurements were obtained each day. In Table IV, we only list A_{UAV}^I and A_{UAV}^A for the antenna constant and C_{UAV}^I and C_{ref}^A for the radar constant. The two radar constants represent the proposed calibration technique and the conventional technique (for most radar, the manufacturer does not provide the antenna pattern but only the specification of the 3-dB beamwidth).

We started the experiment on October 3, 2017, labeled Case 1, and initially, the transmitter power was attenuated with 30 dB to avoid the problem of receiver saturation; however, it turned out to be not a problem with the calibration setting.

We introduced a possible error on the attenuation and the sphere signal-to-noise ratio (SNR) decreased. A large difference in the calculated radar constant from other experiments without attenuation has been found. However, the antenna constant of this campaign can still be used to assess the influence of the antenna approximation on the radar constant estimation. In addition, the external GPS box did not work during the experiment on April 19, 2018 labeled Case 3, which impaired the retrieval of the antenna constants A_{UAV}^I and A_{UAV}^A and the radar constant C_{UAV}^I (they are labeled as not available (NA) in Table IV), but C_{ref}^A could still be calculated.

TABLE IV
CAMPAIGN CONFIGURATION AND RADAR CONSTANT CALCULATION

Case No	Date	Zig-zag direction	Sphere size (cm)	Attenuation (dB)	A_{UAV}^I (dB)	A_{UAV}^A (dB)	C_{UAV}^I (dB)	C_{ref}^A (dB)
1	2017.10.03	horizontal	9	30	32.3	30.8	-205.5	-206.7
		horizontal	13	30	32.3	31.2	-206.0	-207.2
2	2018.03.06	vertical	20	0	32.0	32.1	-201.0	-201.7
		horizontal	20	0	33.1	33.5	-199.8	-201.7
3	2018.04.19	horizontal	20	0	NA	NA	NA	-201.7
		horizontal	20	0	NA	NA	NA	-201.4
		horizontal/vertical	20	0	NA	NA	NA	-202.1
		horizontal	20	0	NA	NA	NA	-201.4
		vertical	27	0	NA	NA	NA	-203.1
		horizontal/vertical	27	0	NA	NA	NA	-203.3
		horizontal/vertical	27	0	NA	NA	NA	-202.4
		horizontal	20	0	32.0	32.1	-199.8	-200.6
4	2018.05.15	vertical	20	0	32.5	32.1	-199.5	-200.8
		horizontal	18	0	32.6	32.5	-200.3	-201.7
		horizontal	18	0	32.6	32.5	-200.3	-201.7
		vertical	18	0	32.1	32.1	-201.0	-201.9

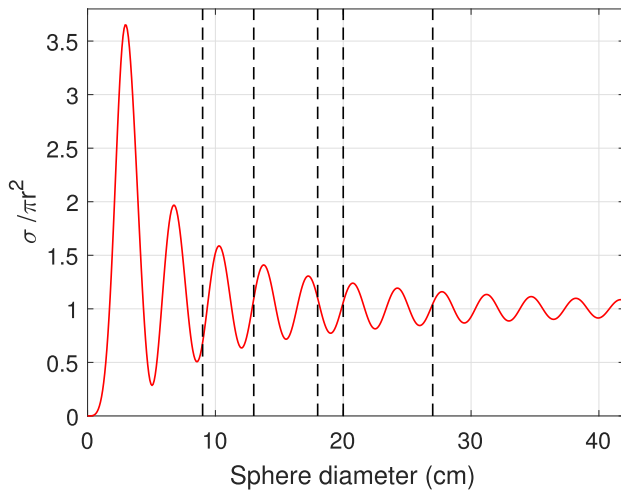


Fig. 9. Sphere diameters versus normalized RCS of metal sphere for S-band TARA.

A. Antenna Constant

As mentioned in Section II-A, the antenna constant can be obtained from the measurements of UAV and transponder. Note that the experiments measuring the antenna beam pattern by using a transponder were conducted 20 years ago, and unfortunately, the data are not available. Based on the report [10], we derive the radar antenna pattern, as shown in Fig. 2. We have $A_{ref}^I = 32.1$ dB and $A_{ref}^A = 31.2$ dB with $\theta_1 = \phi_1$; however, the standard deviation of these measurements cannot be provided. Around 1 dB offset exists when the integration is replaced by the approximation using the specified 3-dB beamwidth in the antenna constant calculation.

In addition, the antenna constants A_{UAV}^I and A_{UAV}^A derived from the UAV measurements can be obtained by the interpolated antenna pattern. Specifically, A_{UAV}^I is calculated by integrating the interpolated antenna pattern and A_{UAV}^A is calculated by taking the 3-dB beamwidth of the interpolated antenna pattern. The antenna pattern fitting is based on the data measured either from horizontal movement (more measurements along the azimuth) or vertical movement (more measurements along the elevation). We consider the interpolated azimuth angles

using the horizontal movement and the interpolated elevation angles using the vertical movement. Optimally, the horizontal and the vertical movement shown in Fig. 7(a) should be implemented to compare the antenna retrieved pattern in azimuth and elevation. This sequence, however, was not carried out in all the cases shown in Table IV. In order to treat all the data the same way, we have to assume the two 3-dB beamwidths equal. Furthermore, due to the lack of the GPS data in Case 3, all the measurements except Case 3 are used to calculate A_{UAV}^I and A_{UAV}^A . Note that data from Case 1 are also involved, because the antenna constants are relative values rather than absolute values (e.g., radar constants).

We display A_{UAV}^I , A_{UAV}^A , A_{ref}^I , and A_{ref}^A together in Fig. 10(a). The mean of A_{UAV}^I is 32.4 dB and the standard deviation is 0.4 dB, while the mean of A_{UAV}^A is 32.1 dB with a standard deviation of 0.8 dB. The antenna constant A_{UAV}^I has a smaller standard deviation than A_{UAV}^A , which is attributed to the integration decreasing the impact of random variation. Therefore, the integration technique is recommended. The mean differences between the UAV derived antenna constants and A_{ref}^I are much less than the differences between the UAV derived antenna constants and A_{ref}^A . Such inter-comparison between the independent measurements demonstrates the advantage of acquiring antenna pattern measurements rather than using the Gaussian approximation with specified 3-dB beamwidth (A_{ref}^A). The agreement between A_{UAV}^I , A_{UAV}^A , and A_{ref}^I indicates the robustness of the proposed UAV-aided methodology.

B. Radar Constant

Before the discussion of the measured radar constants, the theoretical relative error of the radar constant is analyzed using (17). The RCS of the spheres used in the calibration campaigns can be quantified by the anechoic chamber measurements or provided by the manufacturer. Referring to [15], the measured standard deviation of sphere RCS is 0.25 dB, which corresponds to the relative error 5.9%. In our case, we assume that the relative error of the sphere RCS used in the calibration campaigns is the same. The relative error of R_{sp} can be calculated by using the radar-measured range and

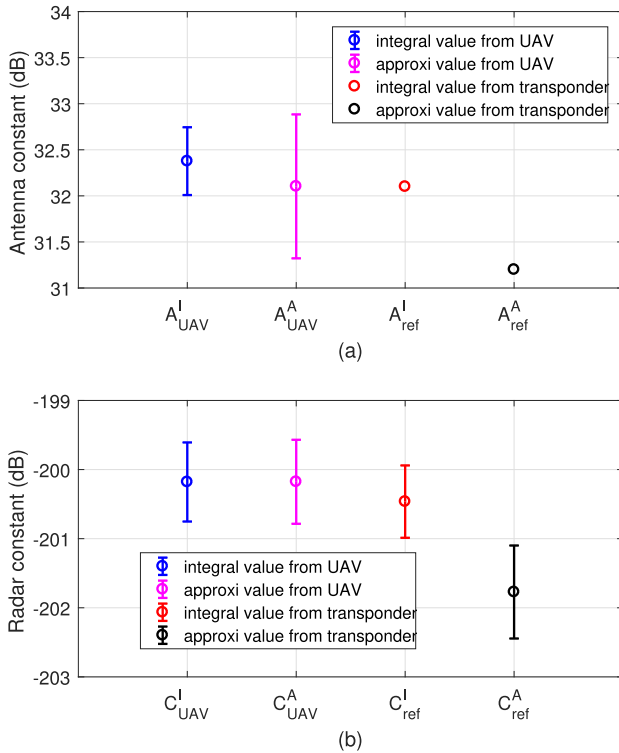


Fig. 10. Experimental results. (a) Antenna constant. (b) Radar constant.

the GPS-retrieved one (an example is shown in Fig. 6), and its value is estimated to be 0.6%. Note that the calibration campaigns were conducted in the condition of weak wind and no precipitation because as mentioned in Section II-B, the wind will influence the sphere positioning accuracy. As for the relative error of $P_{r,sp}^I$, it is related to the SNR. Recall that all the values of $P_{r,sp}^I R_{sp}^4$ larger than 300 dB are considered for the radar constant calculation, which correspond to SNR larger than 30 dB. Therefore, the relative error of $P_{r,sp}^I$ is negligible. Based on the experimental results in Table IV, the relative error of A_{UAV}^I is 8.8%. Last but not the least, the relative error of $r_{L\rho}$ can be quantified, similar to that of A_{UAV}^I , by calculating the standard deviation of several measurements. In this article, the target radar constant is obtained for the radar configured in a high range resolution (the same as the one for radar calibration), so $r_{L\rho}$ equals to 1 and its relative error equals to 0. Overall, the relative error of C_{UAV}^I can be calculated based on (17), and the theoretical standard deviation of C_{UAV}^I is 0.45 dB.

Next, the radar constants C_{UAV}^I , C_{UAV}^A , C_{ref}^I , and C_{ref}^A , which are shown in Fig. 10(b), will be discussed. Specifically, the measurements of Cases 2 and 4 are used to calculate C_{UAV}^I , C_{UAV}^A , and C_{ref}^I , while all the data except Case 1 are used to estimate C_{ref}^A . The mean and standard deviation of C_{UAV}^I are -200.2 and 0.6 dB, respectively, while the mean and standard deviation of C_{ref}^I are -200.5 and 0.5 dB, respectively. In addition, C_{UAV}^A has a mean of -200.2 dB with a standard deviation of 0.6 dB, while C_{ref}^A has a mean of -201.8 dB with a standard deviation of 0.7 dB. It is worth noting that C_{UAV}^I , C_{UAV}^A , and C_{ref}^I have close value distributions. Both C_{UAV}^I and

C_{UAV}^A are obtained based on the retrieved antenna pattern, and they have close value distributions when the antenna pattern has a Gaussian shape. The reason that C_{UAV}^I and C_{ref}^I have similar value distributions is straightforward; both of them are estimated based on antenna pattern integration and the TARA antenna pattern does not seem to have significantly changed in 20 years. The mean difference between C_{UAV}^I and C_{ref}^I is only 0.3 dB, and the mean difference between C_{UAV}^A and C_{ref}^A is 1.6 dB. This further confirmed that the radar constant from the integration is more reliable; namely, C_{UAV}^I and C_{ref}^I are more robust than C_{UAV}^A and C_{ref}^A .

All the radar constants have small standard deviation, within 1 dB, which is obtained by the occasional measurements of seven months. In addition, the spheres used in the experiments have different sizes. These consistencies indicate the reliability of the radar system and no serious anomaly in the RCS of the sphere considered. There is a small difference between the theoretical (0.4 dB) and measured (0.6 dB) standard deviation of C_{UAV}^I . In the analysis of the theoretical standard deviation of C_{UAV}^I , the assumption that the relative error of the sphere RCS is 5.9% is made. When this relative error is increased to 11.7%, the theoretical standard deviation of C_{UAV}^I will also be 0.6 dB. This means that the sphere RCS quantification is necessary for accurate radar calibration.

In summary, these quantitative comparisons and analyses show the good performance of the proposed calibration technique, namely, dual GPS information (UAV and GPS box), range separation of the targets, sphere power integration in the range-Doppler domain, and antenna pattern retrieval and integration.

V. CONCLUSION

This article demonstrates a novel external radar calibration technique—UAV-aided radar calibration. The basic principles and the configuration of the calibration experiments are documented, and the S-band radar TARA is used as the to-be-calibrated radar in this article. Specifically, using a UAV to carry a metal sphere with an external GPS box underneath the sphere, the proper flying modes, namely horizontal and vertical zigzag movements, are designed to intercept the antenna gain pattern at several points. With the GPS coordinates obtained from the UAV and the external GPS box, it is possible to obtain the positions of the sphere and output its azimuth and elevation angles. Then, the antenna pointing calibration can be conducted. Finally, with the radar and GPS measurements, the interpolated 2-D antenna pattern can be retrieved. To quantify the influence of antenna pattern on the radar constant calculation, the antenna constant is defined and it shows that the antenna constant based on the retrieved interpolated antenna pattern is more reliable than the conventional one (i.e., the approximated one). In addition, the calculated radar constants have small standard deviations within 1 dB. These results are based on the usage of different sphere sizes in different experiments. The consistency demonstrates the robustness and effectiveness of the proposed calibration technique.

However, the calibration in this article is not implemented on weather radar in the operational mode (range resolution

should be 30 m instead of 3 m). The main reason is due to the legal UAV flying height limitation in The Netherlands. Now, specific UAV license application for higher flying heights is in progress, and more calibration tests of weather radar in the operational mode can be done in the future. In addition, we propose one way to obtain the radar constant in the operational mode derived from the one calculated at high range resolution. The validation of such technique is underway. In addition, the proposed calibration technique can also be used for cloud radars, most of which have narrow beamwidth (less than 1°) and vertically point to the troposphere. Such work is now under investigation at the Site Instrumental de Recherche par Télédétection Atmosphérique (SIRTA) [16], Palaiseau, France.

ACKNOWLEDGMENT

J. Yin would like to thank the China Scholarship Council for supporting his study at the Delft University of Technology, Delft, The Netherlands.

REFERENCES

- [1] V. N. Bringi and V. Chandrasekar, *Polarimetric Doppler Weather Radar: Principles and Applications*. Cambridge, U.K.: Cambridge Univ. Press, 2001.
- [2] M. A. Richards, J. A. Scheer, and W. A. Holm, *Principles of Modern Radar*. New York, NY, USA: SciTech, 2010.
- [3] E. N. Anagnostou, C. A. Morales, and T. Dinku, "The use of TRMM precipitation radar observations in determining ground radar calibration biases," *J. Atmos. Ocean. Technol.*, vol. 18, no. 4, pp. 616–628, Apr. 2001.
- [4] E. Williams *et al.*, "End-to-end calibration of NEXRAD differential reflectivity with metal spheres," in *Proc. AMS 36th Conf. Radar Meteorol.*, Sep. 2013, pp. 1–17.
- [5] N. Bharadwaj, K. Widener, A. Lindenmaier, and V. Venkatesh, "Calibration system for ARM radars," in *Proc. AMS 36th Conf. Radar Meteorol.*, 2013, pp. 1–7.
- [6] H. Russchenberg and Y. Jiapeng, "Deliverable D2.3: Radar calibration and standardization concepts," in *Proc. Aerosol, Clouds, Trace gases (ACTRIS) workshop*, Oct. 2015, pp. 1–7.
- [7] J.-S. Suh, L. Minz, D.-H. Jung, H.-S. Kang, J.-W. Ham, and S.-O. Park, "Drone-based external calibration of a fully synchronized ku-band heterodyne FMCW radar," *IEEE Trans. Instrum. Meas.*, vol. 66, no. 8, pp. 2189–2197, Aug. 2017.
- [8] S. Duthoit *et al.*, "A new approach for in-situ antenna characterization, radome inspection and radar calibration, using an unmanned aircraft system (UAS)," in *Proc. IEEE Radar Conf. (RadarConf)*, May 2017, pp. 0669–0674.
- [9] A. Freeman, "SAR calibration: An overview," *IEEE Trans. Geosci. Remote Sens.*, vol. 30, no. 6, pp. 1107–1121, Nov. 1992.
- [10] P. Aubry and J. Zijdeveld, "TARA reflector radiation pattern measurements," Int. Res. Center Telecommun. Radar, Delft, The Netherlands, Tech. Rep., 1999.
- [11] J. Yin, C. M. H. Unal, and H. W. J. Russchenberg, "Narrow-band clutter mitigation in spectral polarimetric weather radar," *IEEE Trans. Geosci. Remote Sens.*, vol. 55, no. 8, pp. 4655–4667, Aug. 2017.
- [12] J. Yin, C. Unal, M. Schleiss, and H. Russchenberg, "Radar target and moving clutter separation based on the low-rank matrix optimization," *IEEE Trans. Geosci. Remote Sens.*, vol. 56, no. 8, pp. 4765–4780, Aug. 2018.
- [13] (Aug. 2018). *IGS Network*. [Online]. Available: <http://www.igs.org/network>
- [14] P. F. de Bakker and C. C. J. M. Tiberius, "Real-time multi-GNSS single-frequency precise point positioning," *GPS Solutions*, vol. 21, no. 4, pp. 1791–1803, 2017.
- [15] B. M. Kent, "Comparative measurements of precision radar cross section (RCS) calibration targets," in *Proc. IEEE Antennas Propag. Soc. Int. Symp.*, vol. 4, Jul. 2001, pp. 412–415.
- [16] M. Haeffelin *et al.*, "SIRTA, a ground-based atmospheric observatory for cloud and aerosol research," *Annales Geophysicae*, vol. 23, no. 2, pp. 253–275, 2005.



Jiapeng Yin (S'16) received the B.Sc. degree in information engineering from the National University of Defense Technology (NUDT), Changsha, China, in 2012, and the Ph.D. degree in atmospheric remote sensing from the Delft University of Technology, Delft, The Netherlands, in 2019.

He is currently an Assistant Professor with the College of Electronic Science, NUDT. His research interests include radar polarimetry, polarimetric weather radar, radar signal processing, and radar calibration.



Peter Hoogeboom received the M.S.E. degree in electrical engineering from the Delft University of Technology (TU Delft), Delft, The Netherlands, in 1975.

He started his career after receiving the degree. He worked for more than 40 years in radar remote sensing and instruments. He held several research and management positions. For over ten years, he managed research groups on radar and on remote sensing at TNO, an organization for applied physics research, The Hague, The Netherlands. Since 1999,

he has been a Professor of radar and earth observation with the Delft University of Technology, where he has been involved in instrument studies, and calibration and applications of radars for remote sensing, including atmospheric radar. After his retirement in 2017, he continued part-time work at the Geoscience and Remote Sensing Department, TU Delft, where his experience contributes to a wide range of studies on atmospheric and earth applications of radar.



Christine Unal received the master's degree in physics from the University of Nice Sophia Antipolis, Nice, France, in 1986, and the D.E.A. degree in physics for remote sensing from the University of Paris, Paris, France, in 1987.

In 1988, she joined the Delft University of Technology, Delft, The Netherlands, where she is a currently Research Scientist, where she was with the International Research Center for Telecommunications and Radar and has been with the Department of Geoscience and Remote Sensing and the Climate

Institute since 2012. She started to focus on radar polarimetric calibration and radar spectral polarimetry (quasi-simultaneous Doppler spectra of polarimetric measurements, their processing, and their interpretation). Since 2003, she has applied this expertise to enhance the processing of atmospheric echoes. Her research interests include weather/atmospheric radar signal processing and searching for new retrieval techniques to estimate microphysical and dynamical properties of precipitation using ground-based radars.



Herman Russchenberg is currently the Director of the Climate Institute and the Head of the Department of Geoscience and Remote Sensing, Delft University of Technology (TU Delft), Delft, The Netherlands. He is also a specialist in remote sensing of clouds and precipitation with ground-based radar, lidar, and microwave radiometry. He is experienced in theoretical and experimental research of the scattering process and the retrieval of geo-physical parameters from radar and lidar measurements. He is also one of the leading scientists of the Cabauw Experimental

Site for Atmospheric Research.



Fred van der Zwan was born in The Hague, The Netherlands. He received the Diploma degree from the Electronic Technical School, The Hague, in 1986.

After working at institutes such as Toshiba, TNO, The Hague, The Netherlands, and the Delft University of Technology (TU Delft), Delft, The Netherlands, he became an Electronic Designer at the Telecommunications and Tele-observation Technology Group in 1992. He initiated and coordinates several new radar projects and campaigns. He has

many contacts with all participating partners in several projects. In January 2004, he became the co-applicant of the PARSAX project that was granted in December 2005. After that, he became a Technical Coordinator of the PARSAX Project. In 2010, he became a Technical Coordinator of the Radar Department. In 2017, he became a Drone Pilot. For the TU Delft, he wrote the operational manual and got the certificate to perform drone flights for research purposes.



Erik Oudejans is currently pursuing the master's degree in applied earth sciences with the Department of Geoscience and Remote Sensing, Delft University of Technology, Delft, The Netherlands.

After graduating on the topic of multi-global navigation satellite system (GNSS) single-frequency precise point positioning, he focused on stochastic modeling of range-based observables. His research interests include low-cost position, velocity and time estimation, and satellite remote sensing using deep learning methods.